

UC Berkeley

UC Berkeley Previously Published Works

Title

Constraining Jumps in Density and Elastic Properties at the 660 km Discontinuity Using Normal Mode Data via the Backus-Gilbert Method

Permalink

<https://escholarship.org/uc/item/8vs443st>

Journal

Geophysical Research Letters, 48(9)

ISSN

0094-8276

Authors

Lau, Harriet CP
Romanowicz, Barbara

Publication Date

2021-05-16

DOI

10.1029/2020gl092217

Peer reviewed

1 **Constraining Jumps in Density and Elastic Properties**
2 **at the 660 km discontinuity Using Normal Mode Data**
3 **via the Backus-Gilbert Method**

4 **Harriet C.P. Lau¹, and Barbara Romanowicz^{1,2,3}**

5 ¹Department of Earth and Planetary Science, University of California, Berkeley, CA 94720, USA

6 ²College de France, Paris, France

7 ³Institut de Physique du Globe de Paris, Paris, France

8 **Key Points:**

- 9
- 10 • We use recent normal mode center frequency data to constrain the elas-
11 tic/density properties of the mantle 660 km discontinuity
 - 12 • We find that acceptable range of jumps in P wave-speed and density fall out-
13 side that of standard seismic reference models
 - Our data preclude the global discontinuity being as shallow as 650 km depth

Abstract

We apply the Backus-Gilbert approach to normal mode center frequency data, to constrain jumps in P, S, bulk-sound speed and density at the “660” discontinuity in the earth’s mantle (~ 650 -670 km depth). Different 1D models are considered to compute sensitivity kernels. When using model PREM (Dziewonski and Anderson, 1981) as reference, with a “660” at 670 km depth, the best-fitting jumps in density, P and S wave-speeds range from (5.1-8.2)%, (5.3-8.0)%, (5.0-7.0)%, respectively, so the PREM values lie outside the ranges of acceptable density and P wave-speed jumps. When shifting the depth of “660” to 660 km, the density and S wave-speed jumps increase while the P wave-speed jump decreases. Normal mode data do not support a global transition at 650 km depth. The density jumps are closer to those of pyrolite than PREM while our bulk-sound wave-speed jumps suggest a larger garnet proportion at “660”.

1 Introduction

Phase transitions that occur throughout the mantle greatly affect mantle dynamics and their precise location can provide information about the thermal and compositional variations within the earth. In this study we focus on the so-called “660” discontinuity (hereafter, 660) which has been observed to occur at depths between ~ 650 –670 km, attributed to the transition between the mineral phases ringwoodite/spinel at lower pressures to bridgmanite and oxides at higher pressures (e.g., Birch, 1952; Ringwood, 1991; Shearer, 2000; Shim et al., 2001; Stixrude & Lithgow-Bertelloni, 2005; Frost, 2008). Both seismology and mineral physics have provided important insights into the nature of 660.

Such a phase transition will produce sharp jumps in seismic wave-speed, manifested by seismological observations of reflected phases such as precursors to short period P’P’ phases (e.g., Xu et al., 2003), precursors to SS (e.g., Shearer, 2000) and PP phases (e.g., Deuss et al., 2006), and converted phases as detected in receiver function studies (e.g., Andrews & Deuss, 2008). The depth of the sharp jumps in wave speed listed in seismic reference, spherically symmetric (1D) models vary from 670 km (for PREM, Dziewonski & Anderson, 1981) to 650 km (for STW105, Kustowski et al., 2008), with a currently preferred value of 660 km. At the global scale, the topography of this discontinuity reaches up to ± 30 km (Andrews & Deuss, 2008), with somewhat larger excursions locally, e.g., in subduction zones (e.g., Niu & Kawakatsu, 1995). Observed jumps in S-wave speed, Δv_s , P wave-speed, Δv_p , and in density, $\Delta \rho$, range from 4.5–10.1%, 2.5–5.6%, and 4.2–10.2%, respectively (Montagner & Anderson, 1989; Kennett & Engdahl, 1991; Morelli & Dziewonski, 1993; Estabrook & Kind, 1996; Shearer & Flanagan, 1999; Castle & Creager, 2000). Along with inherent trade-offs between the different physical parameters, the complicated nature of seismic signals observed across the boundary itself must contribute to the wide range of seismically observed jumps (Andrews & Deuss, 2008).

Efforts to combine the mineral physics and seismological approaches aim to tie physical causes to observed seismic properties. For example, by applying equations of states derived from mineral physics, assuming a mantle of adiabatic pyrolite composition, Cammarano et al. (2005) showed that wave-speed jumps that satisfy seismic reference models lay towards the higher end of permissible values from mineral physics constraints. The depth of the discontinuity also provides insights into the non-pyrolitic components (e.g., ilmenite, garnet) within the transition zone (e.g., Vacher et al., 1998; Wang et al., 2006; Ishii et al., 2018).

In this study, we revisit the estimation of globally averaged Δv_s , Δv_p , Δv_b , and $\Delta \rho$ across 660 by applying Backus-Gilbert based methods (Backus & Gilbert,

1970; Pijpers & Thompson, 1992; Masters & Gubbins, 2003) to an extensive recent normal mode catalogue (Roult et al., 2010; Deuss et al., 2013).

2 Data and Methodology

2.1 Data

We use the normal mode center frequencies (and uncertainties) compiled by Robson and Romanowicz (2019) which is based on a combination of the Reference Earth Model catalogue (Laske & Masters, n.d.), observations from Deuss et al. (2013) and radial modes from Roult et al. (2010). The data are provided in Supplementary Table 1.

2.2 Methodology

In a spherical elastic and isotropic earth model, the eigenfrequency ω_k of any isolated normal mode multiplet (denoted by the index k) has distinct sensitivity kernels to v_s , v_p , and ρ structure across the mantle and to topography of any discontinuity, d_i . In the framework of first order perturbation theory, the fractional change in eigenfrequency may be expressed as (e.g. (Woodhouse & Dahlen, 1978)):

$$\frac{\delta\omega_k}{\omega_k} = \int_0^a \left[M_{v_p}^k(r) \frac{\delta v_p}{v_p}(r) + M_{v_s}^k(r) \frac{\delta v_s}{v_s}(r) + M_{\rho}^k(r) \frac{\delta v_{\rho}}{v_{\rho}}(r) \right] dr + \sum_i M_{d,i}^k \delta d_i, \quad (1)$$

where r is the radius and $r = a$ is the surface, $M_{v_p}^k$, $M_{v_s}^k$, M_{ρ}^k are the sensitivity kernels of mode k to perturbations in v_p , v_s , and ρ , respectively. $M_{d,i}^k$ is the sensitivity to topography, d , on the i -th discontinuity.

By considering a linear combination of equation (1) over a set of modes k , we obtain:

$$\sum_k c_k \frac{\delta\omega_k}{\omega_k} = \int_0^a \left[\mathcal{K}_{v_p}(r) \frac{\delta v_p}{v_p}(r) + \mathcal{K}_{v_s}(r) \frac{\delta v_s}{v_s}(r) + \mathcal{K}_{\rho}(r) \frac{\delta v_{\rho}}{v_{\rho}}(r) \right] dr + \sum_i \mathcal{K}_{d,i} \delta d_i \quad (2)$$

where $\mathcal{K}_X = \sum_k c_k M_X^k$ for parameter X which, in this study, $X = v_p, v_s$ or ρ . The coefficients c_k may be determined such that \mathcal{K}_X is designed to enhance the sensitivity of the weighted observations (left-hand side of eq. 2) to a specific region within the mantle and a specific parameter X , while simultaneously reducing the sensitivity to other parameters, Y, Z , and d_i . If the weights \mathbf{c} are successfully determined, in the most ideal case \mathcal{K}_X will be only non-zero across the region of interest, and $\mathcal{K}_Y, \mathcal{K}_Z$ and $\mathcal{K}_{d,i}$ will be zero everywhere. We will refer to both the weighted kernels and data as *composite* kernels and data. An additional condition required of the *composite* kernel is that it should be unimodular:

$$\int_0^a \mathcal{K}_X(r) dr = 1. \quad (3)$$

This is the essence of the Backus-Gilbert methodology. Finding the best combination of data, i.e., finding \mathbf{c} , requires solving an inverse problem and thus carries with it the same regularization issues as in typical geophysical inverse problems.

To expand upon this, we introduce the concept of a *target kernel*, \mathcal{T} , as introduced by Pijpers and Thompson (1992), whose methodology we closely follow (though they considered only one free parameter). \mathcal{T} will be designed such that it follows the shape of the desired sensitivity. Here, we will explore three kernels: (1) a narrow Gaussian centered at 660 (solid black line, Fig. 1a) which is defined as:

$$\mathcal{T}_{\text{full}} = \frac{1}{\Lambda} \exp \left(- \left(\frac{r - r_0}{\Delta} \right)^2 \right) \quad (4)$$

104 where Λ is chosen so that the area under $\mathcal{T}_{\text{full}}$ is 1, Δ is the characteristic width
 105 of the Gaussian centered at $r = r_0$. The remaining two target kernels are trun-
 106 cated versions of this Gaussian, one where the kernel is identical to the full Gaussian
 107 above 660, but is zero below 660, \mathcal{T}_+ (orange kernel, Fig. 1a) and the other where
 108 the kernel is identical to the full Gaussian below 660, but zero above, \mathcal{T}_- (blue ker-
 109 nel, Fig. 1a). The truncated kernels, \mathcal{T}_- and \mathcal{T}_+ , will provide estimates on either side
 110 of the 660, which we will use to determine new jump constraints for ρ , v_p , and v_s .
 111 The full Gaussian, $\mathcal{T}_{\text{full}}$ will provide an overall constraint across the 660 boundary
 112 when testing synthetic models in Section 3.2.

113 In order to determine \mathbf{c} such that the resulting \mathcal{K}_X is as similar to \mathcal{T} as possi-
 114 ble, we minimize the following expression:

$$115 \quad \Phi = \int_0^a [(\mathcal{K}_X - \mathcal{T})^2 + \mathcal{K}_Y^2 + \mathcal{K}_Z^2] dr + \sum_i \mathcal{K}_{d,i}^2 + \mu \sum_{ij} E_{ij} c_i c_j, \quad (5)$$

116 where \mathbf{E} is the covariance matrix of data errors and μ is its corresponding trade-
 117 off parameter. Minimizing Φ with respect to the $(N + 1)$ unknowns, c_j (where
 118 $j = 1, 2, \dots, N$ and N is the number of normal mode center frequencies considered). In
 119 Pijpers and Thompson (1992) they used an additional constraint to ensure that the
 120 area under \mathcal{K} is unity. Here, since \mathcal{T} is designed to be this way, we do not include
 121 this additional constraint. Minimizing Φ with respect to these N unknowns yields N
 122 linear equations which have the form:

$$123 \quad \sum_j \left[\int_0^a M_X^i M_X^j + M_Y^i M_Y^j + M_Z^i M_Z^j dr + \sum_d M_{d,i} M_{d,j} + \mu E_{ij} \right] c_j -$$

$$124 \quad \int_0^a M_X^i \mathcal{T} dr = 0. \quad (6)$$

125 and may be written in matrix form as:

$$126 \quad \mathbf{A} \mathbf{c} = \mathbf{v} \quad (7)$$

127 where $\mathbf{c} = [c_1, c_2, c_3, \dots, c_N]$ and vector \mathbf{v} is

$$128 \quad v_i = \int_0^a M_X^i \mathcal{T} dr \quad (8)$$

129 for $i = 1, 2, \dots, N$. The elements of the $N \times N$ symmetric matrix \mathbf{A} are:

$$130 \quad A_{ij} = \int_0^a M_X^i M_X^j + M_Y^i M_Y^j + M_Z^i M_Z^j dr + \sum_d M_{d,i} M_{d,j} + \mu E_{ij}, \quad (9)$$

131 where $i, j = 1, 2, \dots, N$. Since $\int_0^a \mathcal{T} dr = 1$, an estimate of the quantity of interest, \tilde{X} ,
 132 may be obtained as follows. (Note that in the following expressions we make explicit
 133 any dependence on r and that the “ \sim ” symbol denotes any value integrated over r .)

$$134 \quad \sum_k c_k \frac{\delta \omega_k}{\omega_k} = \int_0^a \frac{\delta X}{X_0}(r) \mathcal{K}_X(r) dr = \left(\frac{\delta X}{X_0} \right), \quad (10)$$

135 where X_0 is the unperturbed depth profile of parameter X from which the kernels
 136 \mathcal{K}_X were determined. Taking $\delta X = X - X_0$, we may write

$$137 \quad 1 + \sum_k c_k \frac{\delta \omega_k}{\omega_k} = \int_0^a \frac{X}{X_0}(r) \mathcal{K}_X(r) dr \quad (11)$$

138 (the value of 1 arising from eq. 3). The radially dependent solution is thus:

$$139 \quad X(r) = X_0(r) \left[1 + \frac{\delta X}{X_0}(r) \right]. \quad (12)$$

140 However, as eq. (10) does not yield radially dependent $\delta X/X_0$, our solution, \tilde{X} , is
 141 an approximation of this (i.e., $\tilde{X} \approx X$) over the radial range for which the kernel is
 142 nonzero (or non-negligible):

$$143 \quad \tilde{X}(r) = X_0(r) \left[1 + \left(\frac{\delta \tilde{X}}{X_0} \right) \right], \quad (13)$$

144 where r is the radius of interest.

145 The uncertainty in the estimate of \tilde{X} , ε , is due to two sources: data error,
 146 ε_{obs} , and contamination from imperfections in the composite kernels, ε_{con} , since in
 147 practice, they will not be fully zero where desired. The contribution from errors in
 148 observation is given by

$$\varepsilon_{\text{obs}}^2 = \mathbf{c} \cdot \mathbf{E} \cdot \mathbf{c}, \quad (14)$$

149 and ε_{con} is due to non-zero contributions from \mathcal{K}_Y , \mathcal{K}_Z and $\mathcal{K}_{d,i}$ (Masters & Gub-
 150 bins, 2003) but also differences between \mathcal{T} and \mathcal{K}_X . This may be estimated by the
 151 following expression

$$152 \quad \varepsilon_{\text{con}}^2 = \int_0^a |\mathcal{K}_X - \mathcal{T}| \varepsilon_X + |\mathcal{K}_Y| \varepsilon_Y + |\mathcal{K}_Z| \varepsilon_Z \, dr + \sum_i |\mathcal{K}_{d,i}| \varepsilon_d, \quad (15)$$

153 where ε_X , ε_Y , ε_Z , and ε_d are uncertainties in the parameters X , Y , Z , and d , respec-
 154 tively, and $|\cdot|$ denotes taking the absolute value.

155 3 Results

156 3.1 Composite Kernels

157 We calculated the sensitivity kernels for each mode to each parameter M
 158 according to Dahlen and Tromp (1998), using the software package MINEOS
 159 (<https://geodynamics.org/cig/software/mineos/>), adopting the widely used seismic
 160 reference model PREM (Dziewonski & Anderson, 1981) as reference. In Section 4.1
 161 we explore the effect of the choice of 1-D reference model.

162 We solve for three separate sets of three kernels $\mathcal{T}_{\text{full}}$, \mathcal{T}_- , \mathcal{T}_+ (Fig. 1a). In
 163 the first set, we enhance sensitivity to ρ and suppress sensitivities to v_p , v_s , and
 164 d_i (Fig. 1b). In Figs 1(c,d) we show the analogous resulting composite kernels for
 165 enhancing sensitivity to v_p and v_s , respectively.

166 While not perfect, the overall shape of the composite kernels \mathcal{K}_X capture \mathcal{T}
 167 very well, with small amounts of noise in all composite kernels (i.e., \mathcal{K}_Y and \mathcal{K}_Z),
 168 which will add to the uncertainty in the estimate.

169 3.2 New Estimates on Jumps

170 In Figs 1(e-g) we show the results obtained by solving eq. (7) successively for
 171 each set of composite kernels. In each figure, it is important to focus on the shift
 172 between the circle and cross, rather than the shift from the PREM profile. Focusing
 173 on the truncated-Gaussian solutions (orange and blue) and the width of the kernel
 174 density bar, it can be seen that for all parameters, the available normal mode data
 175 better constrain the parameter beneath 660 (which is at 670 km in PREM) than
 176 above. For v_s , the PREM values satisfy those of the composite data well (crosses
 177 overlap the circles in Fig. 1g). However, the composite data call for a smaller density
 178 jump (Fig. 1e), and for a larger jump in v_p (Fig. 1f) than in PREM, with shifts both
 179 above and below 660.

180 When one considers averaged values of PREM both above and below 660,
 181 PREM satisfies the composite data for all parameters. This is indicated by the black
 182 circles falling on the black crosses in all panels (Figs 1(e)-(g)).

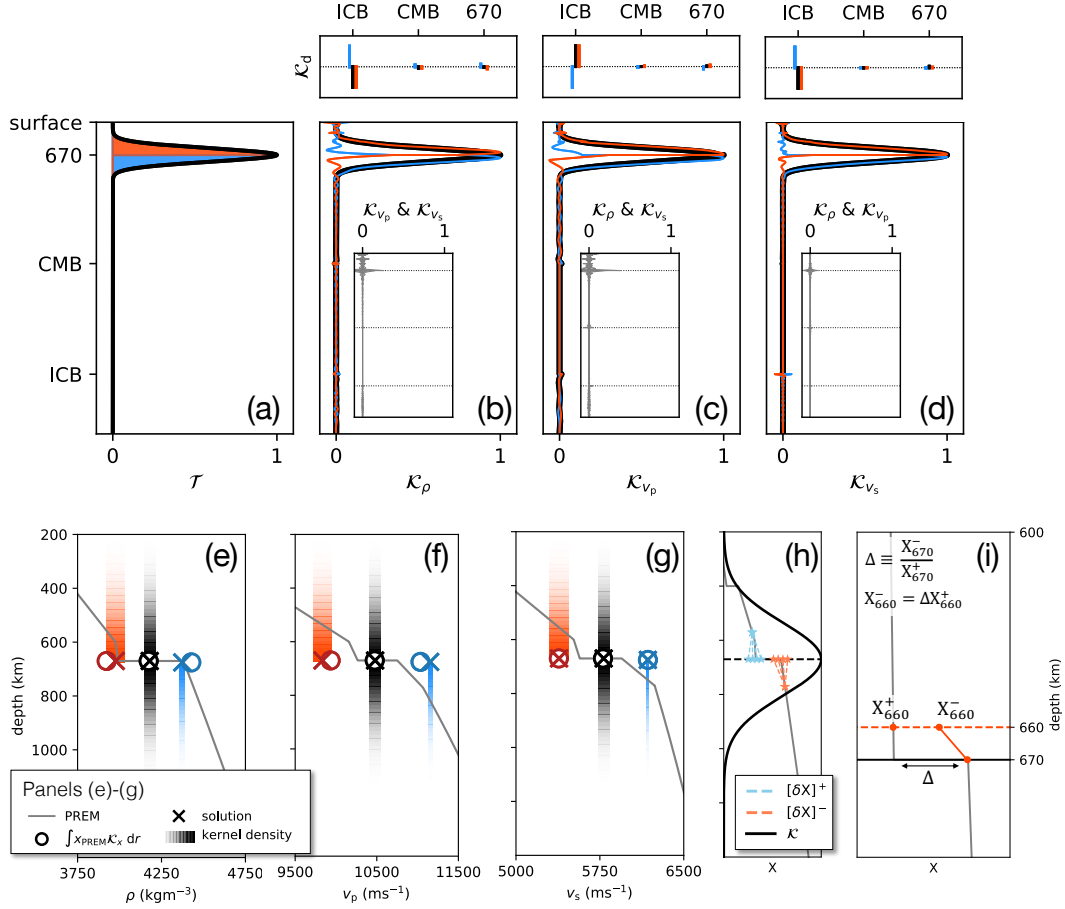


Figure 1. Composite Kernels and Inversion Results. (a) Target kernels for study (blue, \mathcal{T}_- , a half-Gaussian beneath 660; orange, \mathcal{T}_+ , a half-Gaussian above, and black, $\mathcal{T}_{\text{full}}$, a full-Gaussian straddling both beneath and above 660). (b-d) The resulting kernels to enhance sensitivity to ρ , v_p , and v_s , respectively. (In the inset panels, the resulting kernels for the other parameters chosen to be muted). The top panels show relative sensitivity to topography on each discontinuity. (e)-(g) Resulting perturbations in parameters X (where X is ρ , v_p , and v_s in panels (a,b,c), respectively). The circles denote how each kernel samples the background PREM model, while the crosses are the resulting perturbations when applying the composite data. The color intensity of the bar represents the kernel density (see panels b-d). The width of each bar is the uncertainty in the result (eqs 14-15). The gray lines display the PREM profile. (h) A schematic depiction of the test models we consider. The perturbations above and below 660 are guided by solutions shown in panels (e)-(g), and we consider these to increase or decrease linearly from the background PREM model in two cases: 100 km above and below the discontinuity (dashed lines) and 200 km above and below the discontinuity (not depicted). The thick black line is the scaled kernel that is associated with the black bars in panels (e)-(g). This is used as a criterion to exclude test models that do not fit the constraint from the black crosses in (e)-(g). (i) Schematic diagram of how we adjust PREM for a shallower discontinuity at both 660 km and 650 km depth, preserving the percent jump value to that of the standard PREM model. Panels (e)-(h) share the same vertical axes.

183 To explore this further, we tested how these new estimates perform in repro-
 184 ducing the composite data. We perturbed PREM both above and below its 670 km
 185 discontinuity with our new estimates. The values of v_s , v_p and ρ were linearly in-
 186 terpolated to the PREM background model across two length scales: 100 km and
 187 200 km. A schematic depiction of this perturbation is shown in Fig. 1h where we
 188 show test models for the 100 km length scale. These perturbations to the back-
 189 ground model may change the nature of the eigenfrequencies (Dahlen & Tromp,
 190 1998) but re-calculating the eigenfrequencies with these updated models and testing
 191 them against the data is one way to ensure that these models have not changed *too*
 192 much.

193 We produced many perturbed PREM models ($X + \delta X$), choosing values of
 194 parameters above and below the discontinuity within the uncertainty shown in
 195 Figs 1(e-g), applying all possible combinations of ρ , v_p , and v_s . This resulted in
 196 46656 models for each length scale tested. To further scrutinize these models, and
 197 before confronting them with the data, we tested whether these models met the
 198 constraint provided by $\mathcal{T}_{\text{full}}$ (shown in a scaled version in Fig. 1h). This condition
 199 simply requires that the value \bar{X} must lie within the horizontal span of the associ-
 200 ated black colored bar where

$$201 \quad \bar{X} = \int_0^a (X + \delta X) \mathcal{T}_{\text{full}} dr \quad (16)$$

202 and $(X + \delta X)$ is the perturbed model tested. That is,

$$203 \quad (\tilde{X}_{\text{full}} - \varepsilon) \leq \bar{X} \leq (\tilde{X}_{\text{full}} + \varepsilon). \quad (17)$$

204 The result of this additional condition is that none of the models perturbed
 205 across a length scale of 200 km were able to meet the constraint, whereas for the
 206 100 km length scale, 10,000 models satisfied the constraint. Suggesting that any
 207 perturbation from PREM cannot be too wide.

208 For all these results, listed in Fig. 2b, the associated jumps are displayed as
 209 percentages in Fig. 2a, where the final models tested are shown by the blue boxes.
 210 We note that, after the initial culling of models, $\Delta\rho$ and Δv_p are significantly differ-
 211 ent from their respective PREM values. We subject this culled subset of models to
 212 an additional test, as follows. For all models, we predict the set of composite data
 213 and define the chi-squared misfit, χ^2 , as

$$214 \quad \chi^2 = \sum_i \frac{(\Omega_i^{\text{mod}} - \Omega_i^{\text{obs}})^2}{\sigma_i^2}. \quad (18)$$

215 We note that Ω_i is the composite datum from each inversion performed where
 216 $i = [\rho^-, \rho^+, v_p^-, v_p^+, v_s^-, v_s^+]$ and $\Omega_i = \sum_{k=1}^N c_k^i \omega_k$. Indeed, for each parameter i en-
 217 hanced, a different set of coefficients c_k^i is obtained, where k is the index of a mode.
 218 Each inversion is accompanied by a composite uncertainty, σ_i , weighted in the same
 219 manner.

220 We present the misfit reduction, γ , in Figs (3a-d), where γ is the ratio of χ^2
 221 calculated from the test models to χ^2 calculated by PREM. These models corre-
 222 spond only to the perturbed models over a length scale of 100 km, since the 200 km
 223 models did not satisfy the $\mathcal{T}_{\text{full}}$ constraint (eq. 17). They span the blue boxes shown
 224 in Fig. 2a. Trade-offs between wave-speeds Δv_s and Δv_p are shown in Figs 3(a,c),
 225 while trade-offs between wave-speeds Δv_s and Δv_b are shown in Figs 3(b,d). Each
 226 row corresponds to models at two fixed density jumps, where $\Delta\rho$ is 5.1% and 8.2%
 227 for panels (a,b) and (c,d), respectively. These values correspond to the minimum
 228 and maximum $\Delta\rho$ values in the blue boxes of Figure 3.

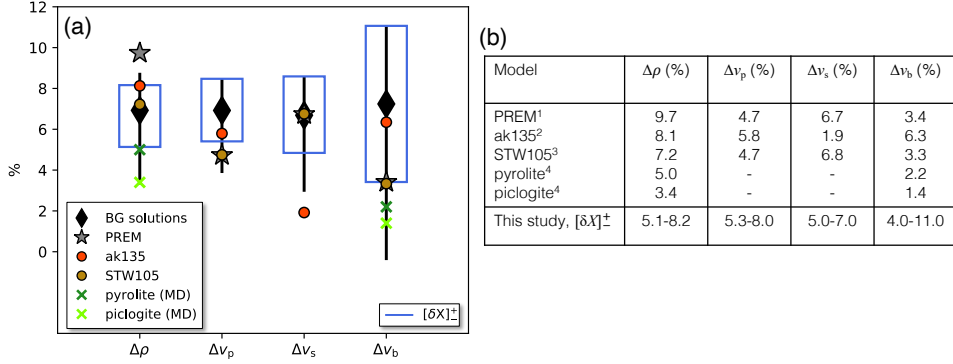


Figure 2. Resulting Jumps Across 660. (a) Black bars (Backus-Gilbert solutions) depict the jumps based on the results Figs 1(e)-(g). The length of the vertical gray lines here corresponds to the width of the colored bars in the latter figure. The blue boxes denote synthetically produced models tested against the data, perturbing PREM above and below the discontinuity over a length scale of 100 km (Fig. 1h). These ranges are less than the gray bars as models that did not satisfy the constraint imposed by $\mathcal{T}_{\text{full}}$ (condition 17) were culled. Symbols represent values from different seismic reference models and from molecular dynamics (MD) calculations. (b) Table of jumps across 660 all listed as percentages. The references for each are as follows: 1: Dziewonski and Anderson (1981); 2: Kennett et al. (1995); 3: Kustowski et al. (2008); 4: Matsui (2000).

229 In the models tested, the misfit was reduced (i.e., $\gamma < 1$) for a significant portion of the models. We see a general preference for lower Δv_s across the range tested and preference for higher Δv_p across the range we test, though these two parameters display some covariance. A trade-off also exists between v_s and v_b , whereby larger values of Δv_s are paired with smaller values of Δv_b .

234 We performed F-tests for all cases at the 99% level of significance (solid red line). For Δv_s , we see that we reach levels of 99% significance in the region of $\sim(4.5-7.5)\%$ for a $\Delta\rho$ of 5.1% and $\sim(5.0-7.5)\%$ for $\Delta\rho$ of 8.2%. As such, we report that these composite data provide revised estimates of these jumps at a 99% significance value of: $\Delta\rho = (5.1-8.2)\%$, $\Delta v_s = (5.0-7.0)\%$, $\Delta v_p = (5.3-8.0)\%$ and $\Delta v_b = (4.0-9.5)\%$, though these ranges are all correlated and should not be taken at face value. The original PREM values are 9.7%, 6.7%, 4.7%, and 3.4%, respectively (see also Fig. 2b).

242 As a further point of comparison, impedance contrasts across 660 are well-constrained by body wave studies (e.g., Shearer & Flanagan, 1999). When comparing v_s and v_p impedance contrasts with SS and PP precursors (as summarized in Deuss, 2009), PREM, pyrolite and piclogite show significantly higher contrasts in both v_s and v_p ($\sim 0.13-0.16$ for both) than body wave-derived estimates ($\sim 0.08-0.11$ in v_s and $\sim 0.05-0.08$ in v_p). (In figure 11 of Deuss (2009), the trade-off between these two quantities is highlighted clearly.) Our v_s and v_p contrasts are 0.08-0.14 and 0.09-0.16, respectively, aligning much closer to PREM and mineral physics values, though do span values close to the upper ends of body wave inferences. It is not clear why the lower frequency normal modes might see a stronger impedance and further investigation is required.

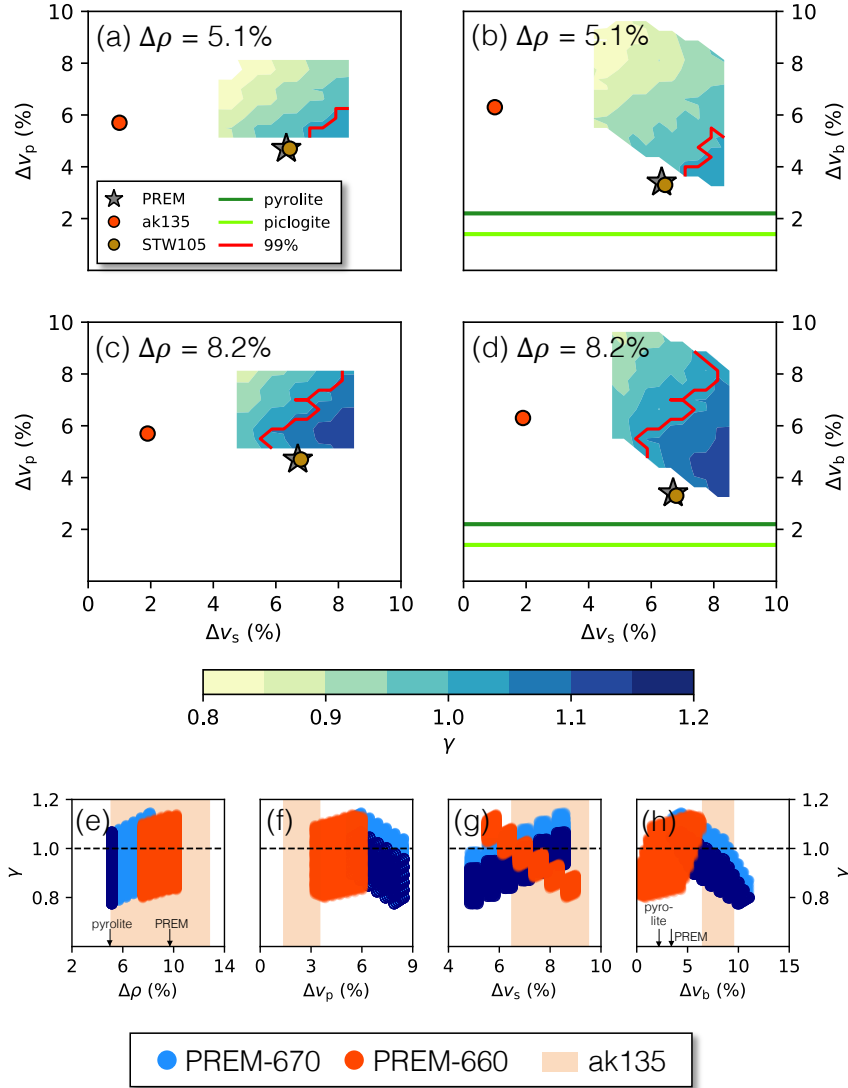


Figure 3. Misfits from Synthetic Tests and Their Trade-Offs. Panels (a-d) display contour plots of the misfit reduction, γ , for models that span the blue boxes in Fig. 2a (i.e., perturbed models over a 100 km length scale). Each row displays models at fixed $\Delta\rho$ values of 5.1% (panels a,b) and 8.2% (panels c,d). These $\Delta\rho$ values span the full range of models that satisfied condition (17). Left panels display trade-offs between Δv_s and Δv_p and right panels display trade-offs between Δv_s and Δv_b . Panels (e-h) show γ for test models that meet the criterion described by condition (17) assuming different background models: the standard version of PREM (blue circles, also shown in panels a-d, where dark blue circles distinguish a subset of these models for which $\Delta\rho$ is the minimum possible density jump of 5.1% highlighting the directionality of trade-offs), PREM in which the discontinuity has been artificially shifted upward to 660 km (orange circles, see Fig. 1e), and assuming the background model ak135 (orange shaded range).

4 Discussion

4.1 Effect of Background Model

In both Figs 2a and 3 we have overlain our results with the corresponding jumps in PREM (gray stars) and the seismological reference models “ak135” (orange circles, Kennett et al., 1995) and “STW105” (yellow circles, Kustowski et al., 2008). While for PREM, the largest differences are seen in $\Delta\rho$ and Δv_p , our results are in much closer agreement with the other two seismic models in $\Delta\rho$ and with ak135 for Δv_p . However, our estimate for Δv_s , while in agreement with PREM and STW105, is substantially different from that of ak135 (which is more than $\sim 2\%$ different). These differences may reflect the fact that that STW105 and PREM were derived from much more similar datasets than ak135, which consisted mainly of short period travel time data sampling the earth’s upper mantle beneath continental areas. We note that no single model shows an obvious consistency with our new estimates for all three parameters.

PREM and ak135 provide a good representation of the range of background models available given the differing nature of the datasets used to produce them. However, another notable difference between these reference models is that PREM places the 660 at a depth of 670 km, whereas ak135 places this discontinuity at 660 km. Here we test how robust our results are to the choice of background model, and specifically, the depth of the 660 in the reference model.

Starting from PREM, we artificially adjusted the discontinuity to two depths: 650 and 660 km. On the upper side of the discontinuity, we kept the PREM parameter values down to the new discontinuity depth. On the underside, we imposed the density and wave-speeds that conserve the original percent jump of PREM for each quantity, in order to isolate the effect of the discontinuity depth. We then linearly interpolated to the original PREM values at 670 km depth (Fig. 1(e)). For each case, we produced new composite kernels, \mathcal{K}_+ , \mathcal{K}_- , and $\mathcal{K}_{\text{full}}$ and repeated the analysis of Sections 2-3.

No model with the discontinuity fixed at 650 km satisfied the condition (17), whereas where the depth of discontinuity was 660 km, 9460 models satisfied this constraint. We show the misfit reduction for the latter distribution of models in Figs 3(e-g) (dark orange circles). For comparison we display the results from the standard analysis (blue circles). By elevating the discontinuity to a shallower depth of 660 km, the trade-offs between Δv_p and Δv_s switch direction, requiring an increase of $\Delta\rho$ and Δv_s and a reduction of Δv_p . Furthermore, it seems that a global average depth of 650 km for the 660 is too shallow to satisfy normal mode data. In line with this, mineral physics experiments of, e.g., Shim et al. (2001) and Ishii et al. (2018), also indicate a deeper depth is favored.

These trade-offs between a shallower discontinuity and increase in both $\Delta\rho$ and Δv_s and a reduction of Δv_p seem to be consistent if we repeat the entire exercise with ak135 (Kennett et al., 1995). We find values corresponding to those of the gray bars in Fig. 2a of (5.1–12.8)%, (1.4–4.3)%, and (6.5–9.5)% for $\Delta\rho$, Δv_p and Δv_s , respectively. The same culling exercise that reduced the gray bars to the dark blue boxes in Fig. 2a (for a perturbation length scale of 100 km) did not result in significant changes to these ranges.

For $\Delta\rho$, the ak135 estimate is similarly poorly constrained relative to the gray bars, but shifted to higher density jumps. For Δv_p and Δv_s the span of the ak135 estimates are roughly two-thirds of the gray bars (compare Fig. 3(e-h) with the black bars in Fig. 2a). In Figs 3(e-h) (orange circles), the misfit reductions of the modified PREM model (with a depth of discontinuity of 660 km, as in ak135) reduce towards the ranges spanned by the ak135 result for all parameters except for Δv_b .

304 These differences between the Backus-Gilbert solutions based on PREM and
 305 ak135 are not trivial, and illustrate the strong non-linearity of the problem, com-
 306 bining the effects of the depth of the discontinuity and of the jumps in the three
 307 parameters considered. Since ak135 was constrained by a very different type of data,
 308 these results likely represent an unrealistic “worst case scenario” when applied to
 309 normal mode center frequency data.

310 4.2 Physical Implications

311 The characteristics of the 660 phase boundary have had much influence on
 312 the conceptual picture of mantle convection. Given that the negative Clapeyron
 313 slope implies that the transition shifts to higher pressures at colder temperatures,
 314 the idea that this transition is a barrier to general mantle circulation has been pro-
 315 posed extensively to satisfy geochemical constraints on mantle heterogeneity (e.g.,
 316 Allègre, 1997) and explored dynamically with consideration to how parameters such
 317 as mantle viscosity might be affected (e.g., van Keken & Ballentine, 1998). While
 318 the picture of mantle convection continues to evolve with better seismic imaging
 319 techniques and more sophisticated modeling capabilities, many of these approaches
 320 require a background seismic model, and, in many cases, PREM is the model of
 321 choice.

322 As such, revising the globally averaged characteristics above and beneath the
 323 660 in the light of recent data is important for both the geodynamical and seis-
 324 mological communities. Paired with increasingly accurate measurements from the
 325 mineral physics literature, a more complete picture of the physical characteristics of
 326 this region will be reached.

327 The mineral physics estimates of Matsui (2000) for $\Delta\rho$ and Δv_b of the model
 328 mantle compositions of pyrolite and piclogite (Ringwood, 1962; Bass & Anderson,
 329 1984) are included in Figs 2a and 3(a-d) (green crosses and lines, respectively). Our
 330 estimates of $\Delta\rho$ are more in line with these mineral physics estimates relative to
 331 PREM, being closer to a pyrolitic composition. This is further visualized in Fig. 3(e)
 332 where misfit reductions point towards the estimate for pyrolite. However, we do not
 333 improve the Δv_b fit to either of these possible compositions (Fig. 3h). It seems from
 334 our results in Section 4.1 that these same conclusions stand whether we consider a
 335 discontinuity at 670 km as in PREM, or 660 km as in ak135.

336 Non-olivine components of the upper mantle, and in particular, the pres-
 337 ence of ilmenite, may affect such jumps across 660 (e.g., Vacher et al., 1998). More
 338 recently, Ishii et al. (2018) explored the transition of ringwoodite to garnet and
 339 magnesiowüstite, as did Wang et al. (2006). The latter found that the large ve-
 340 locity jumps (in NE Asia) may involve a larger fraction of garnet transforming to
 341 perovskite. They also explored how these compositions could affect the velocity gra-
 342 dients surrounding the discontinuity. Our normal mode study cannot resolve these
 343 gradients. Indeed, while our new estimates bring PREM closer to mineral physics
 344 estimates for model mantle minerals, these still lie on the higher end of estimates for
 345 adiabatic pyrolite (Cammarrano et al., 2005).

346 5 Conclusion

347 We have used the Backus-Gilbert method to find a combination of normal
 348 mode center frequency data that enhances sensitivity to just above and below the
 349 660 discontinuity, for density, P wave-speeds, S wave-speeds. We have determined
 350 the best-fitting ranges of jumps in these parameters when assuming PREM as a
 351 background model (Fig. 2b). There is significant covariance between these paramet-
 352 ers. The corresponding PREM value for our $\Delta\rho$ lies above this range, the Δv_p lies

353 below this range, and Δv_s lies within this range. When shifting the depth of 660
 354 to 660 km brings out additional trade-offs resulting in a range of acceptable models
 355 that span larger values of $\Delta\rho$ and Δv_s , and smaller values of Δv_p . In these calcula-
 356 tions, we also found that the normal mode data do not support a globally averaged
 357 phase transition depth as shallow as 650 km depth.

358 Our results produce a range of values for $\Delta\rho$ and Δv_b that are generally higher
 359 than those estimated by mineral physicists for the pyrolite model, and in particular
 360 even higher than PREM for Δv_b , supporting the possibility of a larger proportion
 361 of garnet in the transformation to perovskite. Still, the density jump of PREM is
 362 at the high end of the acceptable models resulting from our study, which may be
 363 important for geodynamicists modeling global convection. Finally, the inability to
 364 obtain a consistent result when using ak135 as a reference model may reflect fre-
 365 quency dependence of structure and/or the presence of significant lateral variations
 366 around the 660.

367 Acknowledgments

368 We thank two anonymous reviewers for providing constructive comments on the
 369 original manuscript. This work was supported by NSF grant EAR-1923865. We
 370 thank Dr Alexander Robson for sharing the compiled normal mode center frequen-
 371 cies (where the data are available through Deuss et al. (2013), Roult et al. (2010),
 372 and Laske and Masters (n.d.)). HL thanks David Al-Attar (University of Cam-
 373 bridge) for some fruitful discussions related to Backus-Gilbert methods.

374 References

- 375 Allègre, C. J. (1997). Limitation on the mass exchange between the upper
 376 and lower mantle: the evolving convection regime of the earth. *Earth*
 377 *and Planetary Science Letters*, 150(1), 1 - 6. Retrieved from [http://](http://www.sciencedirect.com/science/article/pii/S0012821X97000721)
 378 www.sciencedirect.com/science/article/pii/S0012821X97000721 doi:
 379 [https://doi.org/10.1016/S0012-821X\(97\)00072-1](https://doi.org/10.1016/S0012-821X(97)00072-1)
- 380 Andrews, J., & Deuss, A. (2008, June). Detailed nature of the 660 km region of
 381 the mantle from global receiver function data. *Journal of Geophysical Research*
 382 *(Solid Earth)*, 113(B6), B06304. doi: 10.1029/2007JB005111
- 383 Backus, G., & Gilbert, F. (1970, March). Uniqueness in the Inversion of Inaccurate
 384 Gross Earth Data. *Philosophical Transactions of the Royal Society of London*
 385 *Series A*, 266(1173), 123-192. doi: 10.1098/rsta.1970.0005
- 386 Bass, J. D., & Anderson, D. L. (1984, March). Composition of the upper man-
 387 tle: Geophysical tests of two petrological models. *Geophysical Research Letters*,
 388 11(3), 229-232. doi: 10.1029/GL011i003p00229
- 389 Birch, F. (1952). Elasticity and constitution of the earth's interior. *Journal of*
 390 *Geophysical Research (1896-1977)*, 57(2), 227-286. Retrieved from [https://](https://agupubs.onlinelibrary.wiley.com/doi/abs/10.1029/JZ057i002p00227)
 391 agupubs.onlinelibrary.wiley.com/doi/abs/10.1029/JZ057i002p00227
 392 doi: 10.1029/JZ057i002p00227
- 393 Cammarano, F., Deuss, A., Goes, S., & Giardini, D. (2005, January). One-
 394 dimensional physical reference models for the upper mantle and transition
 395 zone: Combining seismic and mineral physics constraints. *Journal of Geophysi-
 396 cal Research (Solid Earth)*, 110(B1), B01306. doi: 10.1029/2004JB003272
- 397 Castle, J. C., & Creager, K. C. (2000, March). Local sharpness and shear wave
 398 speed jump across the 660-km discontinuity. *Journal of Geophysical Research*,
 399 105(B3), 6191-6200. doi: 10.1029/1999JB900424
- 400 Dahlen, F. A., & Tromp, J. (1998). *Theoretical Global Seismology*. Princeton Univer-
 401 sity Press.
- 402 Deuss, A. (2009, October). Global Observations of Mantle Discontinuities Using SS
 403 and PP Precursors. *Surveys in Geophysics*, 30(4-5), 301-326. doi: 10.1007/

- s10712-009-9078-y
- 404 Deuss, A., Redfern, S. A. T., Chambers, K., & Woodhouse, J. H. (2006, January).
 405 The Nature of the 660-Kilometer Discontinuity in Earth's Mantle from Global
 406 Seismic Observations of PP Precursors. *Science*, *311*(5758), 198-201. doi:
 407 10.1126/science.1120020
- 408 Deuss, A., Ritsema, J., & van Heijst, H. (2013, May). A new catalogue of normal-
 409 mode splitting function measurements up to 10 mHz. *Geophysical Journal In-*
 410 *ternational*, *193*(2), 920-937. doi: 10.1093/gji/ggt010
- 411 Dziewonski, A. M., & Anderson, D. L. (1981, June). Preliminary reference Earth
 412 model. *Physics of the Earth and Planetary Interiors*, *25*(4), 297-356. doi: 10
 413 .1016/0031-9201(81)90046-7
- 414 Estabrook, C. H., & Kind, R. (1996, November). The Nature of the 660-Kilometer
 415 Upper-Mantle Seismic Discontinuity from Precursors to the PP Phase. *Sci-*
 416 *ence*, *274*(5290), 1179-1182. doi: 10.1126/science.274.5290.1179
- 417 Frost, D. J. (2008, 06). The Upper Mantle and Transition Zone. *Elements*, *4*(3),
 418 171-176. Retrieved from <https://doi.org/10.2113/GSELEMENTS.4.3.171>
 419 doi: 10.2113/GSELEMENTS.4.3.171
- 420 Ishii, T., Kojitani, H., & Akaogi, M. (2018, January). Phase relations and min-
 421 eral chemistry in pyrolitic mantle at 1600-2200 °C under pressures up to the
 422 uppermost lower mantle: Phase transitions around the 660-km discontinuity
 423 and dynamics of upwelling hot plumes. *Physics of the Earth and Planetary*
 424 *Interiors*, *274*, 127-137. doi: 10.1016/j.pepi.2017.10.005
- 425 Kennett, B. L. N., & Engdahl, E. R. (1991, May). Traveltimes for Global Earth-
 426 quake Location and Phase Identification. *Geophysical Journal International*,
 427 *105*, 429-465. doi: 10.1111/j.1365-246X.1991.tb06724.x
- 428 Kennett, B. L. N., Engdahl, E. R., & Buland, R. (1995, July). Constraints on
 429 seismic velocities in the Earth from traveltimes. *Geophysical Journal Interna-*
 430 *tional*, *122*(1), 108-124. doi: 10.1111/j.1365-246X.1995.tb03540.x
- 431 Kustowski, B., Ekström, G., & Dziewoński, A. M. (2008, June). Anisotropic
 432 shear-wave velocity structure of the Earth's mantle: A global model.
 433 *Journal of Geophysical Research (Solid Earth)*, *113*(B6), B06306. doi:
 434 10.1029/2007JB005169
- 435 Laske, G., & Masters, G. (n.d.). *Reference earth model*. [https://igppweb.ucsd](https://igppweb.ucsd.edu/~gabi/rem.html)
 436 [.edu/~gabi/rem.html](https://igppweb.ucsd.edu/~gabi/rem.html).
- 437 Masters, G., & Gubbins, D. (2003, November). On the resolution of density within
 438 the Earth. *Physics of the Earth and Planetary Interiors*, *140*(1-3), 159-167.
 439 doi: 10.1016/j.pepi.2003.07.008
- 440 Matsui, M. (2000, September). Molecular dynamics simulation of MgSiO₃ per-
 441 ovskite and the 660-km seismic discontinuity. *Physics of the Earth and Plane-*
 442 *tary Interiors*, *121*(1-2), 77-84. doi: 10.1016/S0031-9201(00)00161-8
- 443 Montagner, J.-P., & Anderson, D. L. (1989, December). Constrained reference man-
 444 tle model. *Physics of the Earth and Planetary Interiors*, *58*(2-3), 205-227. doi:
 445 10.1016/0031-9201(89)90055-1
- 446 Morelli, A., & Dziewonski, A. M. (1993, February). Body Wave Traveltimes and A
 447 Spherically Symmetric P- and S-Wave Velocity Model. *Geophysical Journal In-*
 448 *ternational*, *112*(2), 178-194. doi: 10.1111/j.1365-246X.1993.tb01448.x
- 449 Niu, F., & Kawakatsu, H. (1995). Direct evidence for the undulation of the 660-
 450 km discontinuity beneath tonga: Comparison of japan and california ar-
 451 ray data. *Geophysical Research Letters*, *22*(5), 531-534. Retrieved from
 452 <https://agupubs.onlinelibrary.wiley.com/doi/abs/10.1029/94GL03332>
 453 doi: <https://doi.org/10.1029/94GL03332>
- 454 Pijpers, F. P., & Thompson, M. J. (1992, September). Faster formulations of the
 455 optimally localized averages method for helioseismic inversions. *Astronomy and*
 456 *Astrophysics*, *262*(2), L33-L36.
- 457 Ringwood, A. E. (1962, February). A Model for the Upper Mantle. *Journal of Geo-*

- 459 *physical Research*, 67(2), 857-867. doi: 10.1029/JZ067i002p00857
- 460 Ringwood, A. E. (1991, August). Phase transformations and their bearing on the
461 constitution and dynamics of the mantle. *Geochimica et Cosmochimica Acta*,
462 55(8), 2083-2110. doi: 10.1016/0016-7037(91)90090-R
- 463 Robson, A. J. S., & Romanowicz, B. (2019, October). New normal mode constraints
464 on bulk inner core velocities and density. *Physics of the Earth and Planetary
465 Interiors*, 295, 106310. doi: 10.1016/j.pepi.2019.106310
- 466 Roult, G., Roch, J., & Clévéde, E. (2010, March). Observation of split modes from
467 the 26th December 2004 Sumatra-Andaman mega-event. *Physics of the Earth
468 and Planetary Interiors*, 179(1-2), 45-59. doi: 10.1016/j.pepi.2010.01.001
- 469 Shearer, P. M. (2000, January). Upper mantle seismic discontinuities. *Washington
470 DC American Geophysical Union Geophysical Monograph Series*, 117, 115-131.
471 doi: 10.1029/GM117p0115
- 472 Shearer, P. M., & Flanagan, M. P. (1999). Seismic velocity and density jumps across
473 the 410- and 660-kilometer discontinuities. *Science*, 285(5433), 1545-1548.
474 Retrieved from <https://science.sciencemag.org/content/285/5433/1545>
475 doi: 10.1126/science.285.5433.1545
- 476 Shim, S.-H., Duffy, T. S., & Shen, G. (2001, May). The post-spinel transformation
477 in Mg_2SiO_4 and its relation to the 660-km seismic discontinuity. *Nature*,
478 411(6837), 571-574.
- 479 Stixrude, L., & Lithgow-Bertelloni, C. (2005, August). Thermodynamics of mantle
480 minerals - I. Physical properties. *Geophysical Journal International*, 162(2),
481 610-632. doi: 10.1111/j.1365-246X.2005.02642.x
- 482 Vacher, P., Mocquet, A., & Sotin, C. (1998, April). Computation of seismic profiles
483 from mineral physics: the importance of the non-olivine components for ex-
484 plaining the 660 km depth discontinuity. *Physics of the Earth and Planetary
485 Interiors*, 106(3-4), 275-298. doi: 10.1016/S0031-9201(98)00076-4
- 486 van Keken, P. E., & Ballentine, C. J. (1998). Whole-mantle versus layered man-
487 tle convection and the role of a high-viscosity lower mantle in terrestrial
488 volatile evolution. *Earth and Planetary Science Letters*, 156(1), 19 - 32.
489 Retrieved from [http://www.sciencedirect.com/science/article/pii/
490 S0012821X98000235](http://www.sciencedirect.com/science/article/pii/S0012821X98000235) doi: [https://doi.org/10.1016/S0012-821X\(98\)00023-5](https://doi.org/10.1016/S0012-821X(98)00023-5)
- 491 Wang, Y., Wen, L., Weidner, D., & He, Y. (2006, July). SH velocity and compo-
492 sitional models near the 660-km discontinuity beneath South America and
493 northeast Asia. *Journal of Geophysical Research (Solid Earth)*, 111(B7),
494 B07305. doi: 10.1029/2005JB003849
- 495 Woodhouse, J. H., & Dahlen, F. A. (1978, 05). The Effect of A General Aspherical
496 Perturbation on the Free Oscillations of the Earth. *Geophysical Journal Inter-
497 national*, 53(2), 335-354. Retrieved from [https://doi.org/10.1111/j.1365-
498 -246X.1978.tb03746.x](https://doi.org/10.1111/j.1365-246X.1978.tb03746.x) doi: 10.1111/j.1365-246X.1978.tb03746.x
- 499 Xu, F., Vidale, J. E., & Earle, P. S. (2003, January). Survey of precursors to P'P':
500 Fine structure of mantle discontinuities. *Journal of Geophysical Research
501 (Solid Earth)*, 108(B1), 2024. doi: 10.1029/2001JB000817